CEAS Aeronautical Journal
https://doi.org/10.1007/s13272-025-00837-y

ORIGINAL PAPER

Airframe noise simulation of an A320 aircraft in landing configuration

Stan Proskurov[1] · **Michael Moessner**[1] · **Roland Ewert**[1] · **Jan W. Delfs**[1] · **Juergen Dierke**[1] · **Michael Pott-Pollenske**[1] · **Daniela Almoneit**[1]

Received: 4 October 2024 / Revised: 26 February 2025 / Accepted: 25 March 2025

Abstract

The high-lift system noise is predicted for a landing approach condition for the actual scale Airbus 320-232 "D-ATRA" research aircraft of DLR. Noise simulations are performed for all key elements of the high-lift wing using stochastically derived sources, based on the underlying one-off Reynolds-Averaged Navier–Stokes CFD simulation. Turbulence quantities that are essential for the acoustic source characterisation are derived from the CFD solution by means of eddy viscosity. The acoustic perturbation equations (APE) are solved in close proximity to the aircraft using a volume-resolving discontinuous Galerkin method, valid in a non-uniform medium, assuming uncorrelated source domains. Then, the acoustic data are collected on a permeable Ffowcs Williams and Hawkings (FWH) surface and integrated to a far-field, where the acoustic pressures from different sources are combined for obtaining the overall noise footprint. The aeroacoustic simulation is compared to fly-over measurements in a blind test setting. A very good agreement is reported for the overall sound pressure level (OASPL) predictions.

Keywords Airframe noise · Acoustics · Noise modelling · Advanced simulation · Turbulence

List of symbols

c_0	Speed of sound at infinity
c_l	Length scale coefficient
c_p	Specific heat capacity at const. p
c_λ	Enstrophy scaling coefficient
$\boldsymbol{f}'$	Fluctuating force vector
i, j	Einstein notation
$\tilde{k}_t$	Mean turbulent kinetic energy
l_s	Turbulence length scale
$l_{\min}$	Cut-off turb. length scale
n	Dimension, 3 for 3D
p'	Acoustic pressure
$q_c;\boldsymbol{q_m}$	Acoustic sources
$\boldsymbol{r}$	Relative separation
$s;s'$	Entropy and its fluctuation
t	Time
$\boldsymbol{u}'$	Acoustic velocity vector
$\boldsymbol{u_0}$	Mean flow velocity vector
$\boldsymbol{u}^r$	Rotational velocity vector
$\tilde{u}_i$	Favre averaged velocity component
$\boldsymbol{x};\boldsymbol{x}'$	Position vectors
A	Fluctuating velocity-based source
A^n	Source amplitude function
B	Fluctuating vorticity-based source
C_μ	RANS scaling constant
G	Gaussian function
$\mathcal{R}$	Two-point space–time correlation
$\tilde{S}$	Stress–strain rate
T	Temperature
T_p	Time period
$\mathcal{U}$	Stochastic field
V_s	Source integration volume
γ	Adiabatic coefficient
δ	Dirac delta function
ζ	Enstrophy
$\theta;\phi;r$	Spherical coordinates
μ	Mean dynamic viscosity
$\tilde{\nu}$	Mean kinematic viscosity
$\tilde{\nu}_t$	Mean turbulent eddy viscosity
ρ_0	Mean flow density
σ_k	Eddy relaxation parameter
τ	Temporal separation
ψ'	Fluctuating stochastic stream function
$\boldsymbol{\omega}$	Vorticity vector

✉ Stan Proskurov
stanislav.proskurov@dlr.de

[1] Department of Technical Acoustics, Institute of Aerodynamics and Flow Technology, German Aerospace Center (DLR), Lilienthalplatz 7, 38108 Brunswick, Germany

$\boldsymbol{\omega}_0;\tilde{\boldsymbol{\omega}}_t$	Mean vorticity vector; derived
$\boldsymbol{\omega}'$	Vorticity fluctuation vector

1 Introduction

In Europe, the Advisory Council for Aviation Research (ACARE) demands a 65% reduction of the perceived noise per operation by 2050, relative to the 2000 baseline [1]. Achievement of the Vision target depends on many factors, which include modelling and simulation technologies, their integration into multi-disciplinary design loops, and versatile optimisation processes, aimed at individual components and complete air vehicles. In this paper, we demonstrate our simulation technology readiness level by predicting airframe noise for an A320 "baseline" commercial aircraft, which had been accomplished in the framework of an internal DLR project SIAM. Fly-over tests and array measurements were conducted in May 2016 [2] for the D-ATRA A320-232 research aircraft of DLR (see Fig. 1). Then, Pott-Pollenske et al. [3] carried out a noise reduction study, where various elements of the high-lift system, such as slat and flap side edges were identified as intense sources of airframe noise. Therefore, a landing approach testing point with fully deployed high-lift devices was selected for the simulation. The flight speed of the ATRA aircraft was 135 kt. at a flight altitude of 600 ft. over the measurement area, with several passes recorded. For those low-altitude fly-overs, the recorded pitch angle was approximately −1° and the flow angle of attack (AoA) was estimated to be 4.5° that was matched in a CFD simulation, performed using the unstructured flow solver TAU [4].

Aeroacoustics simulations for a full aircraft gained recognition mainly via the application of a lattice Boltzmann method at NASA. In 2014, Khorrami, Fares, and Casalino [5] showed airframe noise predictions for an 18%-scale Gulfstream aircraft model. Later, Appelbaum et al. [6] followed the same approach to compute airframe noise for a full-scale Gulfstream aircraft, and in 2021, Khorrami et al. [7] obtained airframe noise predictions for a more challenging Boeing 777-300ER large aircraft configuration from their lattice Boltzmann simulation. All of the above require big resources and access to a large computational facility. For instance, DLR is in partnership with the ProLB [8] (lattice Boltzmann software) consortium with access to the solver, but it would have been problematic allocating resources for a full-scale aircraft for the duration of the project, without special priorities. Also, the application of lattice Boltzmann methods for optimisation remains several orders of magnitude too high in terms of the CPU-hours per cycle, in respect of industry standards. Therefore, at the SIAM project kick-off meeting, the decision was taken to model all noise sources independently, using the appropriate stochastic source reconstruction techniques. Several source definitions of varying complexity are applied in this work, starting from a vorticity source of the fast random particle mesh (FRPM) method [9] to a more accurate representation of turbulence noise sources, where all aspects relating to production, diffusion, dissipation, advection, and fully 3D anisotropic behaviour are taken into account [10]. In essence, the evolution of turbulence kinetic energy is solved in the form of a transport equation using a zonal approach. The equation is explicitly advanced in time using an appropriate CFL condition, which is independent of the speed of sound but related to a background flow. The methodology allows for absolute level predictions, as well as for low noise optimisation of different airframe components inside of a global computational aeroacoustics domain. In the past, synthetic turbulence sources were successfully derived from mean flow for components of a high-lift system (e.g., by Reiche et al. [11], full scale), but up to date never for such a complicated mix of noise mechanisms, combined in a simulation dedicated to predicting acoustics of a full A320 aircraft in a landing

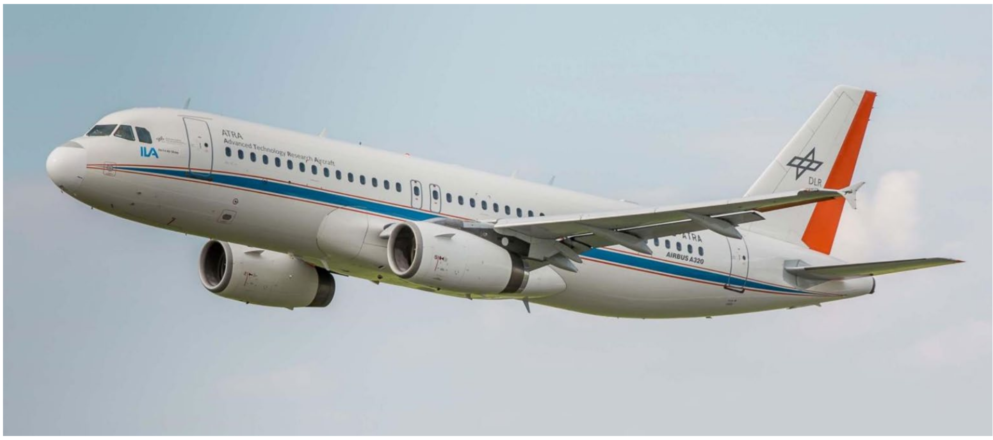

Fig. 1 D-ATRA during flight tests in Cochstedt, Germany. DLR©

configuration. Figure 2 shows the sources of noise broken down into key regions where a case number and name are assigned for reference. In Sect. 4.2.3, it is explained why some outboard slat tracks are not numbered but their contribution to noise is considered. The sources are propagated through a non-uniform but steady time-averaged aerodynamic background flow field in a volume-resolving discontinuous Galerkin simulation, where the acoustic perturbation equations (APE) [12] are employed on the wave propagation side. The Ffowcs Williams and Hawkings (FWH) [13] integration is used to extrapolate the acoustics from a near far-field to observer microphones, accounting for the Mach number difference in between. After obtaining the acoustic prediction for the far-field, the data were compared to fly-over measurements and the results are shown at the end of this paper, but, first, the method is discussed.

2 Noise source models

The noise mechanisms triggered by turbulence are complicated as can be seen from Lighthill's analogy, which source terms do not have a simple physical meaning except for the simplest cases of sound generation in a uniform stationary medium. Therefore, it would be impossible to prescribe the noise sources for the A320 under consideration based on analytical formulations. The sources have to be derived from the governing flow equations with an accurate representation of aircraft's geometry. It is often desirable to apply some noise theory where equations of motion for a compressible fluid are rearranged in a way to completely separate the linear propagation effects. Hence, the underlying acoustic formulation used in this work is the APE system, which has proven to be numerically stable for various discretisation schemes, and which consists of equations describing acoustic pressure and velocity

$$\frac{\partial p'}{\partial t} + c_0^2 \nabla \cdot \left(\rho_0 \boldsymbol{u}' + \boldsymbol{u_0} \frac{p'}{c_0^2} \right) = c_0^2 q_c \tag{1}$$

$$\frac{\partial \boldsymbol{u}'}{\partial t} + \nabla \left(\boldsymbol{u_0} \cdot \boldsymbol{u}' \right) + \nabla \left(\frac{p'}{\rho_0} \right) = \boldsymbol{q_m}, \tag{2}$$

where the right-hand side sources of the APE-4 variant [12] are provided from an exact rearrangement of the Navier–Stokes equations in disturbance form, defining an acoustic analogy based on the APE equation system

$$q_c = -\nabla \cdot \left(\rho' \boldsymbol{u}' \right)' + \frac{\rho_0}{c_p} \frac{D_0}{Dt} s' \tag{3}$$

$$\boldsymbol{q_m} = -(\boldsymbol{\omega} \times \boldsymbol{u})' + (T \nabla s)' - \left(\nabla \frac{(u')^2}{2} \right)' + \left(\frac{\nabla \cdot \underline{\boldsymbol{\tau}}}{\rho} \right)', \tag{4}$$

where the sound is generated by vorticity, viscous stresses, and entropy inhomogeneities. In the above equations, terms with a prime after parentheses refer to the quantity in parentheses with a subtracted mean. $D_0/Dt = \partial/\partial t + \boldsymbol{u_0} \cdot \nabla$ denotes the substantial time derivative, and $\boldsymbol{u_0}$ and $\boldsymbol{u}'$ are the mean flow velocity vector and its fluctuation. The variables T and s are temperature and entropy in accordance with the standard definitions used in thermodynamics, $\underline{\boldsymbol{\tau}}$ stands for the stress tensor, and c_p is the specific heat capacity at constant pressure. The speed of sound, $c_0 = \sqrt{\gamma p_0/\rho_0}$ obeys the ideal gas law, $\gamma = 1.4$, and the remaining quantities

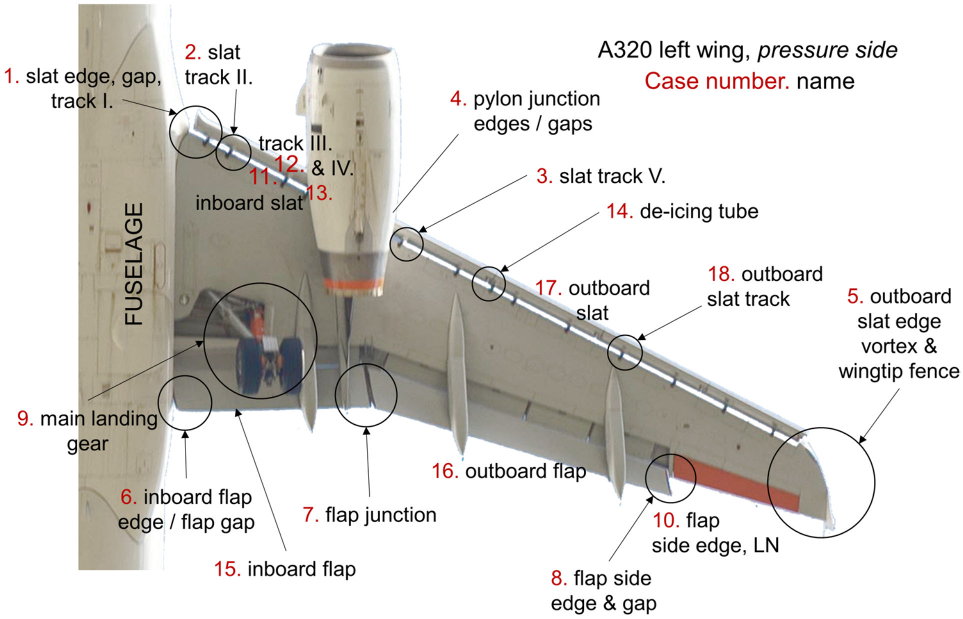

Fig. 2 Photograph of the D-ATRA high-lift system DLR©; CAA simulation strategy: noise sources

have their usual meaning. As observed by Powell [14], the sound generation in subsonic flows with a constant entropy assumption is associated with the vortex dynamics. Indeed, if the non-linear and entropy terms are considered of minor importance, the major remaining vortex source term from Eqs. (3)–(4) is the Lamb vector, $-(\boldsymbol{\omega} \times \boldsymbol{u})'$. Typically, the effective vortex sound source is evaluated with the help of additional simplifying assumptions, where the Lamb vector can be expressed through the following three terms:

$$\boldsymbol{q_m} \approx -(\boldsymbol{\omega} \times \boldsymbol{u})' = \underbrace{-\{\boldsymbol{\omega_0} \times \boldsymbol{u}'\}}_{\mathrm{I}} \underbrace{-\{\boldsymbol{\omega}' \times \boldsymbol{u_0}\}}_{\mathrm{II}} \underbrace{-\{\boldsymbol{\omega}' \times \boldsymbol{u}'\}}_{\mathrm{III}} . \tag{5}$$

The first two terms in Eq. (5) represent linear sources with respect to the velocity and vorticity fluctuations, and the third one is quadratic in terms of the fluctuations, which is thought to be a lot smaller than the first two terms at low Mach numbers and by assumption is usually neglected. As discussed by Ewert et al. [9], it is often the second, vorticity fluctuation term included, whilst the rest of the sources are ignored. This vortical description should then be understood as the right-hand side source, which *only together with an appropriate acoustic propagation formulation and boundary conditions becomes the true acoustic source*.

When the Lamb vector components in Eq. (5) are derived from a time-averaged flow, e.g., using stochastic methods, the vorticity-less formulation in Eqs. (1)–(2) with localised sources may turn out to be insufficient for problems where the vorticity transport plays a role. Some examples include capturing propeller installation effects or simulating cavity flows, where a proper representation of vortex sheets is important. It is worth mentioning that some sources may be formulated for other sets of linear, e.g., linearised Euler (LEE), or even non-linear equations, which by default incorporate both vortical and pure acoustic modes. One way to account for vorticity convecting in a velocity field is by referring to a generalised hydrodynamic-acoustic splitting (HAS) approach [15]. The other way of the flow acoustics splitting was derived for the combination of CAA with a compressible RANS flow [10]. The latter approach offers some additional advantages on the numerical side, such as a straight forward extension of Eqs. (1)–(2), making the acoustic propagation part coupled to a vortex transport equation. In that variant, the perturbation velocity is split up into an irrotational (pure acoustic) part, here still referred to as $\boldsymbol{u}'$, and a residual part $\boldsymbol{u^r}$ that contains the complete vorticity. The residual part is not divergence-free, $\nabla \cdot \boldsymbol{u^r} \neq 0$, and with such splitting completely describes the fluctuating vorticity, $\boldsymbol{\omega}' := \nabla \times \boldsymbol{u^r}$. The split set of equations with incorporated vorticity mode reads

$$\frac{\partial p'}{\partial t} + c_0^2 \nabla \cdot \left(\rho_0 \boldsymbol{u}' + \boldsymbol{u_0} \frac{p'}{c_0^2} \right) = -c_0^2 \nabla \cdot \left(\rho_0 \boldsymbol{u^r} \right) \tag{6}$$

$$\frac{\partial \boldsymbol{u}'}{\partial t} + \nabla \left(\boldsymbol{u_0} \cdot \boldsymbol{u}' \right) + \nabla \left(\frac{p'}{\rho_0} \right) = 0 \tag{7}$$

$$\frac{\partial \boldsymbol{u^r}}{\partial t} + (\boldsymbol{u_0} \cdot \nabla)\boldsymbol{u^r} + (\boldsymbol{u^r} \cdot \nabla)\boldsymbol{u_0} = -(\boldsymbol{\omega_0} \times \boldsymbol{u}') + \boldsymbol{f}', \tag{8}$$

where Eq. (8) introduces the vorticity mode coupled via the divergence of $\boldsymbol{u^r}$ to the acoustic perturbation equations (APE), as can be seen from the right-hand side of Eq. (6). Also, the acoustic equations provide feedback into the vorticity mode in Eq. (8) via the curl of mean vorticity with the acoustic velocity. Notice that the feedback term is only relevant for rotational mean flow regions. The forcing term appears on the right-hand side of the vortical flow equation, where, in general, the system of split equations (6)–(8) is equivalent to the LEE system with a non-linear source term. However, the LEEs are known to suffer from numerical instabilities, including fatal global instabilities and will only work robustly with an eddy relaxation term (ERT) that provides the necessary dissipation mechanism. In 2016, Ewert [16] published a concept of a stochastically forced linear advection–diffusion–dissipation (FLAD) equation based on the RANS-model partial differential equation for turbulent kinetic energy. The concept was further developed in [10], demonstrating the application of the model to highly anisotropic turbulent flow structures found in a tip gap leakage flow. The right-hand side forcing term of Eq. (8) incorporates stochastic fluctuations that are shaped to represent a properly scaled coloured noise, which must conform to an energy spectrum of choice. The turbulent forcing is specified together with ERT, $(\tilde{\nu} + \sigma_k \tilde{\nu}_t)$ which ensures that the turbulence production from forcing balances in magnitude the turbulent dissipation (acting on $\boldsymbol{u^r}$), leading to energy redistribution into different wavenumbers in the energy cascade

$$\boldsymbol{f}' = \nabla \times \left[(\tilde{\nu} + \sigma_k \tilde{\nu}_t) \left\{ \nabla \times \left(\boldsymbol{u^r} - \boldsymbol{u}'_{REF} \right) \right\} \right]. \tag{9}$$

Above, $\sigma_k \approx 0.85 \ldots 1$ is the relaxation parameter and $\boldsymbol{u}'_{REF}$ is derived from stochastic fluctuations. The transport equation for $\boldsymbol{u^r}$ with the above forcing term reads

$$\begin{aligned} &\frac{\partial \boldsymbol{u^r}}{\partial t} + (\boldsymbol{u_0} \cdot \nabla)\boldsymbol{u^r} + (\boldsymbol{u^r} \cdot \nabla)\boldsymbol{u_0} + \nabla \times \left[(\tilde{\nu} + \sigma_k \tilde{\nu}_t) \left(\nabla \times \boldsymbol{u^r} \right) \right] \\ &\quad = -(\boldsymbol{\omega_0} \times \boldsymbol{u}') + \nabla \times \left[(\tilde{\nu} + \sigma_k \tilde{\nu}_t) \left(\nabla \times \boldsymbol{u}'_{REF} \right) \right]. \end{aligned} \tag{10}$$

In practise, $\tilde{\nu}$ is expected to be several orders of magnitude smaller than $\tilde{\nu}_t$ and simply using $\sigma_k \tilde{\nu}_t$ factor on both sides could be a reasonable approximation after verifying it for any case of interest. Overall, the usage of ERT ensures that any spurious noise is suppressed, which could be generated in a formulation that is not divergence free. The above equation could be solved in a separate sub-domain or directly on a CAA grid. The forcing term should be enabled not only at the source location but also downstream to properly represent the turbulence cascade.

3 Stochastic sources based on eddy viscosity

One way to efficiently derive the fluctuating components of the Lamb vector in Eq. (5) without having to solve the Navier–Stokes equations in a time-resolving simulation is via a stochastic approach, such as the FRPM method [17]. The classical FRPM is based on spatial filtering of white noise, weighted with a local turbulent kinetic energy and length scale from a RANS solution, aiming to generate fluctuations of meaningful cross-correlation and strength. In this project, the fly-over CFD simulation was performed for a complete A320 aircraft in "landing gear down" configuration with the Spalart–Allmaras one equation turbulence model with rotation curvature correction (SA-RC), which is an industry standard way of obtaining reliable aerodynamic solutions. However, the SA model provides only one turbulence parameter, which is the turbulent eddy viscosity $\tilde{\nu}_t$. The eddy viscosity is insufficient on its own, meaning that the turbulent kinetic energy that is required for proper scaling is then obtained via Bradshaw's hypothesis, which states that the Reynolds shear stress is proportional to the turbulent kinetic energy [18]. First, time-averaged flow gradients are evaluated by the CFD solver for improved discretisation accuracy. Second, the divergence of mean velocity $\nabla \cdot \boldsymbol{u_0}$ is obtained, followed by the stress tensor $\tilde{S}_{ii}$:

$$\tilde{S}_{ii} = \nabla \tilde{u}_i - (\nabla \cdot \boldsymbol{u_0})/3. \tag{11}$$

The $\tilde{S}_{ii}$ makes up the diagonal of a 3×3 matrix where the strain components $\tilde{S}_{ij}$ are evaluated to fill up the remaining slots

$$\tilde{S}_{ij} = \frac{1}{2}\left(\frac{\partial \tilde{u}_i}{\partial x_j} + \frac{\partial \tilde{u}_j}{\partial x_i}\right) \quad i \neq j; \tag{12}$$

$$\tilde{S} := \sqrt{2\left(\sum_{i=1}^{3} \tilde{S}_{ii}\tilde{S}_{ii} + \sum_{ij;\ i\neq j} \tilde{S}_{ij}\tilde{S}_{ji}\right)}. \tag{13}$$

In Eq. (13), $\tilde{S}$ is the stress–strain rate tensor, which is defined to fulfil the relationship between turbulent eddy viscosity $\tilde{\nu}_t$ and turbulent kinetic energy, $\tilde{k}_t$ [19]

$$\tilde{k}_t = \frac{\tilde{\nu}_t \tilde{S}}{\sqrt{C_\mu}}, \tag{14}$$

where $C_\mu = 0.09$. The turbulence length scale is computed from eddy viscosity $\tilde{\nu}_t$ and $\tilde{k}_t$ using the following relationship:

$$l_s = \frac{c_l}{C_\mu}\frac{\tilde{\nu}_t}{\sqrt{\tilde{k}_t}} = \frac{c_l}{\sqrt{C_\mu}}\frac{\sqrt{\tilde{k}_t}}{\tilde{S}}. \tag{15}$$

In Eq. (15), $c_l := 0.5$, which is kept constant throughout the domain.

Stochastic sources are required to locally reproduce the two point space–time correlation $\mathcal{R}(\boldsymbol{x}, \boldsymbol{r}, \tau) = \langle \psi(\boldsymbol{x}, t)\psi(\boldsymbol{x} + \boldsymbol{r}, t + \tau)\rangle$ of a stochastic fluctuating stream function $\psi(\boldsymbol{x}, t)$ of a continuous convolution, where for n-dimensional space, the filtering integral reads

$$\psi(\boldsymbol{x}, t) = \int_{V_s^n} \hat{A}^n(\boldsymbol{x}')\, G\big(|\boldsymbol{x} - \boldsymbol{x}'|, l_s(\boldsymbol{x}'))\big)\mathcal{U}(\boldsymbol{x}', t)\mathrm{d}\boldsymbol{x}'. \tag{16}$$

Several strategies can be pursued from this point onwards for obtaining the acoustic source. For example, the fluctuating vorticity in the second term of Eq. (5) could be simulated directly by associating it with the fluctuating stream function vector, such as $\boldsymbol{\psi} \sim \boldsymbol{\omega}'$, which is one of the most uncomplicated and robust ways. This is sometimes referred to as *Source B* realisation [9]. Then, in Eq. (16), the filter amplitude $\hat{A}$, becomes a function of the local enstrophy [20]. The source (volume) region in which unsteady sources are generated is denoted V_s, and G is the Gaussian filter kernel that is a function of a separation distance $|\boldsymbol{x} - \boldsymbol{x}'|$. A recursive implementation of the Gaussian filter is used (see Young and van Vliet [21]). The integral length scale $l_s(\boldsymbol{x}') := l_{\min}$, in *Source B* becomes position-independent, meaning that in Eq. (15) the value of c_l is only nominal, which helps to determine the order of l_s. Then, the smallest length scale of interest is chosen inside V_s. Thus far, the focus has been on spatial properties controlled by the Gaussian filter, where, for *Source B*, the smallest length scale is proportional to the filter width. On the other hand, temporal properties of turbulence are solely controlled by the stochastic field $\mathcal{U}$. For example, convection effects of the white noise field must be considered and could be described via a spatiotemporal correlation, which covariance results in a delta function: $\langle \mathcal{U}(\boldsymbol{x}, t)\mathcal{U}(\boldsymbol{x} + \boldsymbol{r}, t + \tau)\rangle \rightarrow \delta(\boldsymbol{r} - \boldsymbol{u_0}\tau)\mathcal{R}(\tau)$. Here, τ is a relative separation time and $\boldsymbol{r}$ is a multi-dimensional distance vector, e.g., in 3D, $\delta(\boldsymbol{r}) = \delta(r_1)\delta(r_2)\delta(r_3)$. In short, the unique spatiotemporal white noise field properties can be summarised as follows:

$$\langle \mathcal{U}(\boldsymbol{x}, t)\rangle = 0 \tag{17}$$

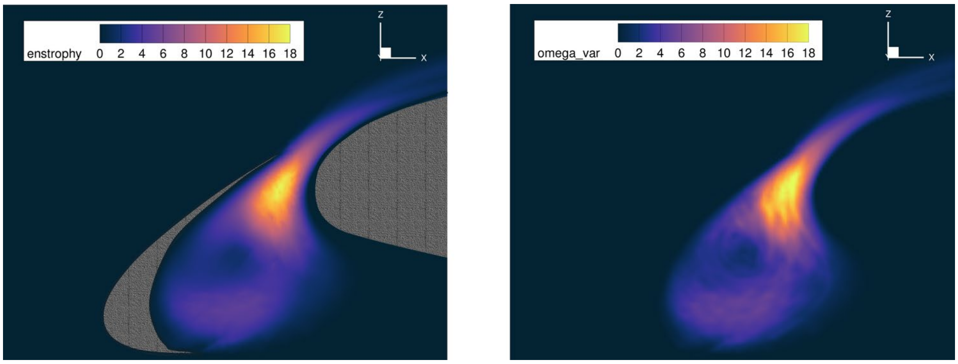

Fig. 3 Enstrophy obtained from RANS via Eq. (20) (left) and mean vorticity variance from stochastic fluctuations (right)

$$\langle \mathcal{U}(\boldsymbol{x},t)\mathcal{U}(\boldsymbol{x}+\boldsymbol{r},t+\tau)\rangle = \delta(\boldsymbol{r}-\boldsymbol{u_0}\tau)\mathcal{R}(\tau) \tag{18}$$

$$\frac{D_0}{Dt}\mathcal{U} \neq 0. \tag{19}$$

On the right-hand side of Eq. (18), $\mathcal{R}(\tau)$ is a temporal correlation, where the idea is to relate the characteristic time of evolving turbulence to the temporal scale of relaxation of the turbulent fluctuations, which ultimately results in Eq. (19) condition. The concept of eddy relaxation can be important for some problems, which is incorporated into a more advanced version, namely the forced linear advection dissipation equation. In the classical FRPM, however, turbulence is convected frozen by assumption, meaning that the integral time scale of turbulence tends to infinity and the autocovariance of $\mathcal{U}$ becomes independent of the temporal separation τ, resulting in the stochastic field that passively convects with a mean flow $\boldsymbol{u_0}$, and remains locally static. For frozen turbulence: Eq. (17) of vanishing mean holds, the right-hand side of Eq. (18) simply becomes a multi-dimensional delta function with a mean flow convection $\delta(\boldsymbol{r}-\boldsymbol{u_0}\tau)$, and the substantial time derivative in Eq. (19) equals zero.

In Ref. [20], it was described how enstrophy ζ can be used instead of turbulent kinetic energy in a stochastic turbulence region, representing the accumulation of vorticity fluctuations. Enstrophy is a convenient measure used for scaling *Source B*, since the fluctuating stream function is directly associated to vorticity fluctuations. More specifically, it is scaled with $l_{\min}$ to fit the grid resolution

$$\zeta = 20\cdot\frac{c_\lambda}{l_{\min}}\,\frac{\tilde{k}_t}{c_0^2\, l_{\min}^2}. \tag{20}$$

In the above equation, the coefficient c_λ is based on the ratio of kinematic viscosity to specific turbulence dissipation rate

$$c_\lambda = \sqrt{10\cdot\frac{\tilde{\nu}}{\tilde{\omega}_t}}, \tag{21}$$

where $\tilde{\nu}$ is the kinematic viscosity, $\tilde{\nu} = \tilde{\mu}/\tilde{\rho}$ and $\tilde{\omega}_t = \tilde{k}_t/\tilde{\nu}_t$ is the specific turbulence dissipation rate. Notice that in Eq. (20), c_0^2 is used to get the dimensionless $\tilde{k}_t$. The amplitude scaling is defined by assuming isotropic correlation $\mathcal{R}(\boldsymbol{x},0,0) \propto \frac{\zeta}{3}$, which then reads

$$\hat{A}^n(\boldsymbol{x}') = \sqrt{\frac{\rho_0\mathcal{R}}{l^n_{\min}}} = \sqrt{\frac{\rho_0\cdot\zeta}{3\,l^3_{\min}}}. \tag{22}$$

All mean quantities required for the stochastic model have been derived and it is important to verify that the one-point statistics from RANS can be reproduced. Figure 3 shows slices which are aligned with the x-axis at the inboard slat of the left wing, extracted for Case #11 in Fig. 2, where the flow is in the positive x-direction. This is a useful check for *Source B*, where one can visualise time-averaged vorticity fields alongside the corresponding enstrophy input. High values of enstrophy indicate where noise sources are found.[1]

4 Aeroacoustic simulation

A CFD grid, consisting of 244 million unstructured cells, was designed in the (DLR) TFZ department for obtaining the mean flow solution at the Reynolds number of $\approx 20\times10^6$. However, a best practise RANS grid is generally unsuitable for unsteady aeroacoustics computations. Since the flow is obtained for a complete aircraft and the acoustic near-field is computed on top of the mean flow, it is possible to consider only one side from symmetry with a much reduced far-field, without sacrificing the quality of aeroacoustic predictions. Figure 4 highlights the process of airframe noise modelling via the FRPM method. A more sophisticated FLAD model discussed in Eq. (10) will only change the CAA formulation

---

[1] Stochastic source simulation is performed locally, in 3D on a Cartesian grid with boundary conditions prescribed by the mean flow, which explains the absence of solid wall shading for the reconstructed vorticity variance.

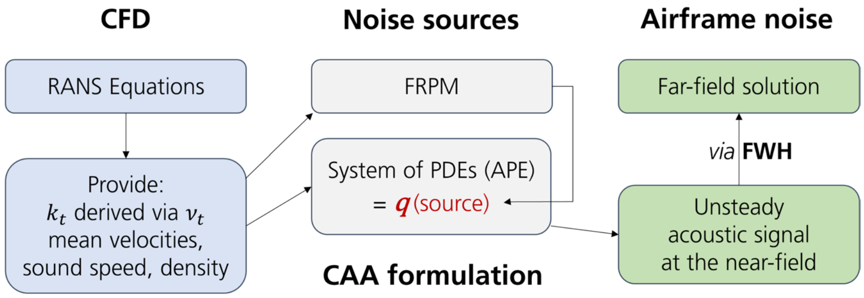

Fig. 4 Diagram of a hybrid CFD/CAA approach where airframe noise sources are obtained via the FRPM method

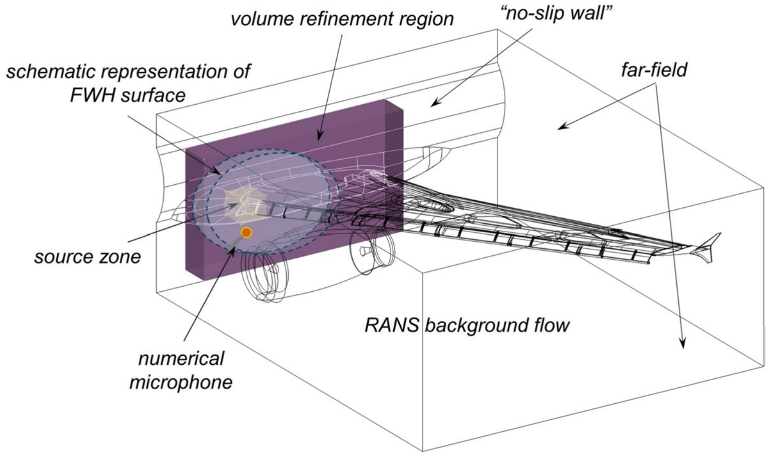

Fig. 5 CAA domain; the half aircraft sketch is used for visualisation purpose only, and it resembles the D-ATRA aircraft but is not the true A320 geometry

and how the stochastic forcing is used, but the same process is followed.

The CAA domain shown in Fig. 5 includes a high-lift wing, engine, and parts of fuselage, which is a sub-domain of a much bigger RANS domain. To keep simulations efficient, a fixed size domain is used with adjustable mesh refinement around the source region—the remaining volume features a gradual mesh coarsening towards far-field boundaries. There are ≈ 200 k unstructured surface faces per single simulation run with the volume resolution of ≈ 0.006 m at the source. The refinement region supports frequencies up to 4 kHz and distant noise sources are assumed to be fully uncorrelated, which allows investigating into noise sources on individual basis. This is very convenient for noise reduction study, because noise footprints can be produced for isolated components or groups, such as for inboard or outboard slat, or for flaps and edges but without slats or landing gear. See Table 1 for simulated cases and parameters.

4.1 Inboard slat

4.1.1 Slat edge, gap, and track I

The sources are enclosed by an FRPM box, where *source B* is used in every slat noise simulation. Figure 6 shows the instantaneous acoustic pressure exerted on the surface and iso-surfaces of vorticity, computed from acoustic velocities that are caused by stochastic sources. Notice the long streaks of the iso-surface that pass through the gap at the root of the wing. The start and end points correspond to the boundaries of the FRPM box.

As previously discussed, the fluctuating stream function of *source B* is based on $l_{\min}$ and it is clearly visible that acoustic velocities (and vorticities) are anisotropic, which is an important feature in slat cove/slat gap noise modelling. A numerical microphone is placed 1 m below the slat hook edge to get an idea of noise content in the near field. The FFT signal looks meaningful with a low frequency peak and a gradual decay, capturing all of the slat hook noise and decaying naturally beyond 2 kHz, within the grid resolution limit. Due to a very fine time step of the propagator, the FWH data were sampled only once per 100 acoustic steps. It is ensured that the variation of a raw pressure signal is smooth for the finest time interval, such that no meaningful data are lost when employing less frequent write operations. Figure 7 shows a randomly selected microphone from a far-field array of numerical microphones for Case #11. This check ensures that all frequencies with significant amplitudes are resolved, the signal stays within bounds and even for the shortest time window—smooth fluctuations are recorded.

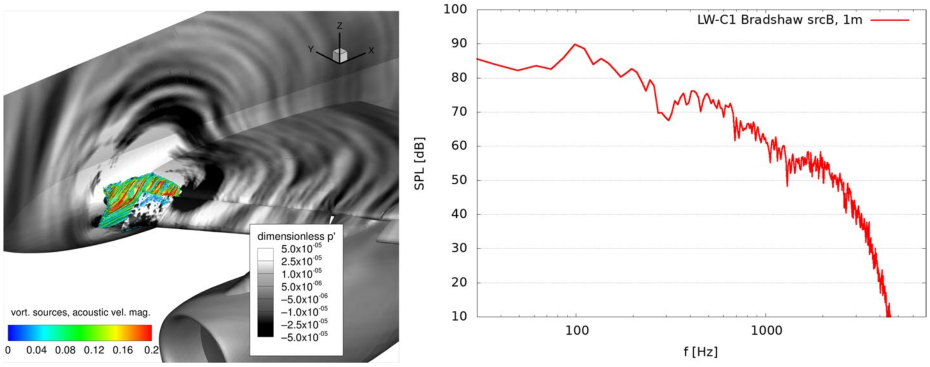

Fig. 6 Acoustic pressure and iso-surface of vorticity (left); raw SPL narrowband spectrum at 1 m below the slat edge (right)

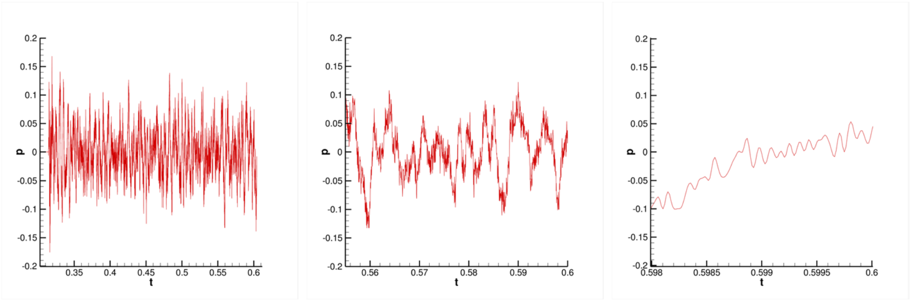

Fig. 7 Far-field numerical microphone at 100 m, plane centre: raw pressure data

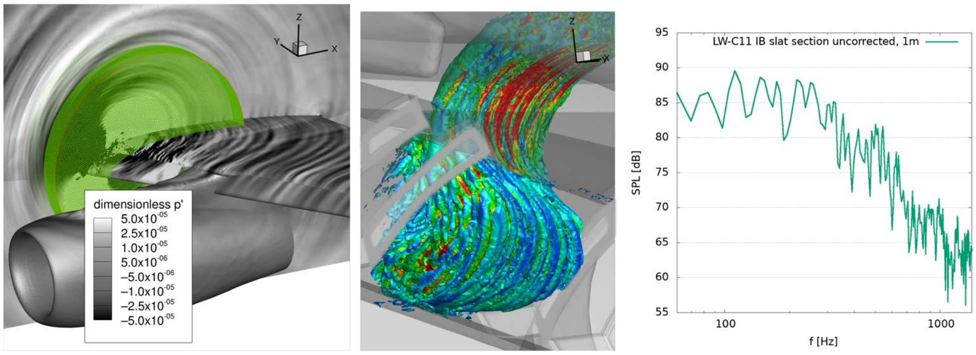

Fig. 8 Case 11 left to right: acoustic pressure and FWH surface; Q-criterion coloured by fluctuating velocity magnitude; uncorrected near-field SPL narrowband spectrum, i.e., representing the effective source volume

4.1.2 Slat tracks II, III, and IV

The remaining tracks of the inboard slat are also modelled with *source B*. The distance between tracks II and III is significantly larger than between I and II or III and IV, which will be close to pure slat noise evaluation. The pure slat noise source is modelled with a finite 3D extent of 0.6 m and a spanwise correction is then applied between source regions of tracks II and III to properly account for the actual extent of the inboard slat. Unfortunately, flow appears to be different around each of the four slat tracks, mostly because it is influenced by presence of the fuselage, engine, gaps, and edges of the high-lift system. Therefore, it is impossible to rely on similarity principles and all four tracks have to be simulated. Figure 8 shows the acoustic evaluation for the inboard slat, from left to right: contours of acoustic pressure and local FWH surface, Q-criterion in the slat gap region—view from the underside with translucent airframe, and a sample of SPL spectrum at 1 m, which shows the importance of low frequencies ≈ 100–400 Hz. The spectrum is derived from a raw sample for the effective source volume, which has not been corrected for the slat extent between the other two volume source zones (slat track II and III).

Figure 9 shows slices along the inboard slat for independently simulated slat tracks. The slat tracks produce noise levels in a similar range, but differences can be identified on a plane or hemi-sphere, and thus, it is well worth computing each one of them for an improved accuracy.

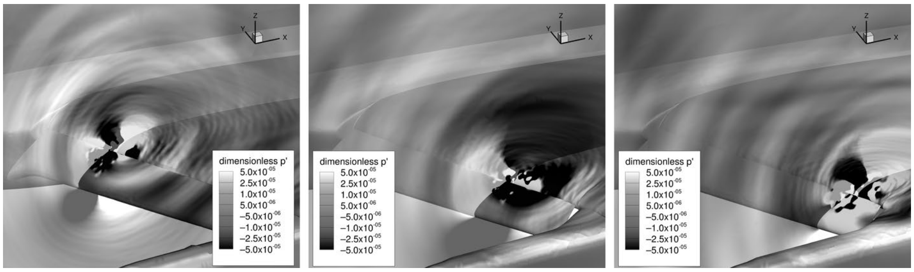

Fig. 9 Acoustic pressure contours for uncorrelated noise sources of tracks II, III, and IV

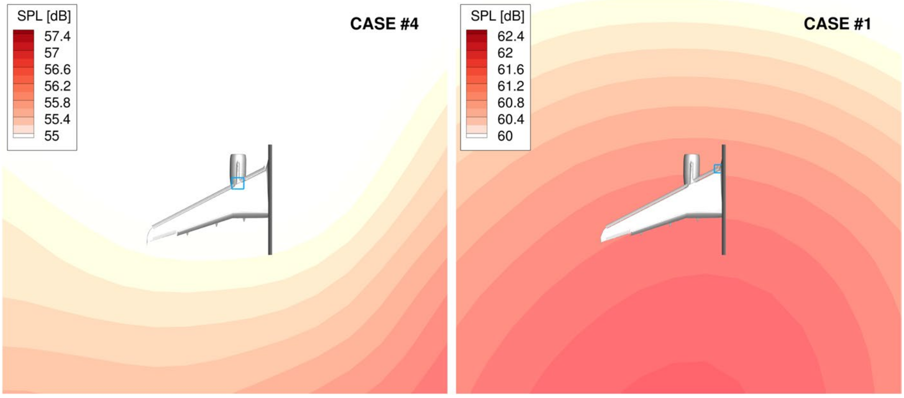

Fig. 10 SPL [dB] footprints on a large plane below the aircraft from the simulation with flow: "wind tunnel scenario"

4.1.3 Pylon junction

The zonal simulation of pylon junction includes two adjacent slat edges. At first glance, it may seem that these two slat edges could be major contributors to noise. However, in the simulation, we get strong noise shielding for Case #4, as shown in Fig. 10, where the narrowband SPL ground levels for the pylon junction are significantly lower than for Case #1 (root of the wing) or for any other inboard slat track. The noise directivity is also very different, where the edges close to the pylon radiate downstream and sideways, more so in the direction of the fuselage.

On the other hand, the slat edge, gap, and track I radiate predominantly downstream. The plane in Fig. 10 is similar to a wind tunnel scenario with a fixed source, observer, and having flow convection in between.

4.2 Outboard slat

This is an important element that contributes to overall noise in landing configuration, primarily due to its sheer size and spanwise extent. Assume that a typical patch width for a slat source is ≈ 0.6 m. If the slat track and edge zones are subtracted from the overall outboard slat width, one could estimate the "clean slat extent" which for an A320 is just over 7 m. Then, applying the spanwise SPL correction to far-field noise $+10\log_{10}(\text{slat extent}/\text{patch width}) \approx +11\,\text{dB}$. For example, the simulation of Case #17 (clean outboard slat section with 0.6 m span) produced an uncorrected peak level of 62.1 dB on a plane at $z = -100$ m, which together with the above correction brings it up to 73.1 dB for all clean outboard slat segments but without considering edges and tracks.

4.2.1 Slat track V

This slat track belongs to the outboard slat and is the closest one to the engine. The CAA requirement was to have a good quality CFD mesh in the slat cove, to avoid large uncertainties for calculated or computed turbulence kinetic energy and turbulence dissipation rate. That applies particularly to flow computed around the slat track V, because we noticed that turbulence kinetic energy could be overly dissipated on a grid which employs quick coarsening away from the wall. The TKE at the inner slat surface close to the gap was affected and that is where noise sources are found. Therefore, it took a fair amount of effort to validate the RANS via grid refinement and attempting to reproduce turbulence statistics with a two-equation model by switching from SA to $k-\omega\ SST$. However, the two-equation model converged poorly due to other unrelated areas, such as detached flow around the main landing gear. It was then attempted to converge the k-equation in an unsteady mode but keeping the converged mean velocities from SA fixed. There were no convergence problems with the SA model on an improved grid from which the flow was used for source modelling. Figure 11 shows an acoustic snapshot based on the Bradshaw (SA model) source.

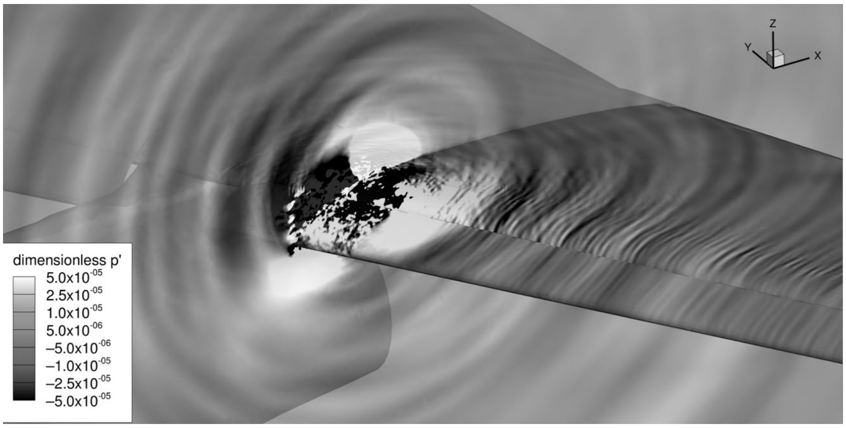

Fig. 11 Acoustic pressure contours for slat track V, case #3

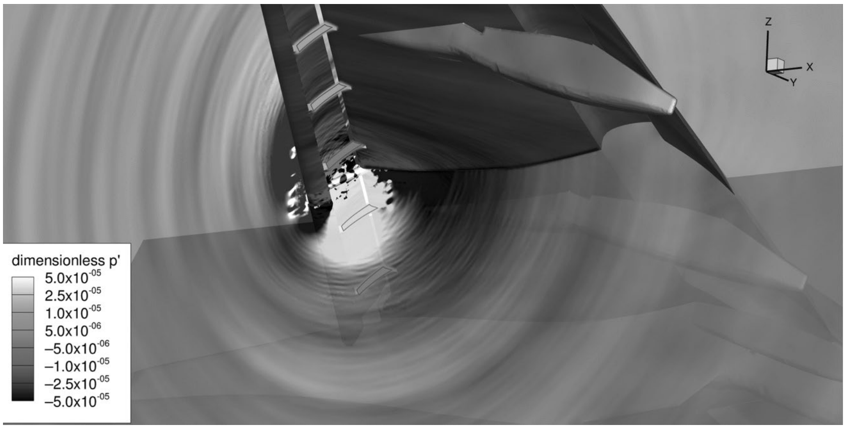

Fig. 12 Acoustic pressure contours around the de-icing tube, case #14

4.2.2 De-icing tube

This device is handled similarly to other slat tracks in terms of source definitions and mesh resolution. In terms of the far-field noise, the de-icing tube produces similar radiation pattern to an outboard slat track, case #18 but is marginally quieter, with a peak level of 62.1 dB on the $z = -100$ m plane as opposed to 62.7 dB for the outboard slat track and 64.15 dB for the slat track V, case #3. All slat sources, including tracks and the de-icing tube radiate downstream at $\approx 110° \ldots 115°$. The acoustic waves propagating in the near-field are shown in Fig. 12.

4.2.3 Outboard slat track

Up to this point, each prominent slat source region was simulated because even for the neighbouring zones the flow may have slightly different features. However, the averaged flow around identical slat tracks located in the middle of the outboard slat is very similar, and therefore, it is possible to cut down on 6 simulations by summing up the acoustic contributions of case #18. From quick test simulations and acoustic sampling in the near-field, it was possible to estimate that the overall noise will not vary by more than 1dB between simulated and summed up cases, which is well within the uncertainty. Also, some stronger sources will make this uncertainty irrelevant when contributions from all sources are accounted for. Figure 13 shows contours of acoustic pressure for the outboard slat track and the nearby “clean slat” noise case #17. As far as far-field noise is concerned, the slat track case #18 produced $+\Delta 0.7$ dB on the $z = -100$ m plane at the peak location for an identical volume and slat extent in comparison to the “clean slat” case #17. The difference is not as striking as for the wing root gap or even the slat track V; nevertheless, the noise increase caused by slat tracks was clearly detected when post-processing far-field data, meaning that slat tracks of the outboard slat must be taken into account.

4.3 Slat side edge and wingtip fence

The flow physics of the slat side edge and wingtip fence involves complicated interaction mechanisms for which the stochastic *source B* model comes short and is typically lacking high-frequency content. Therefore, we switch to the canonical stochastic forced linear

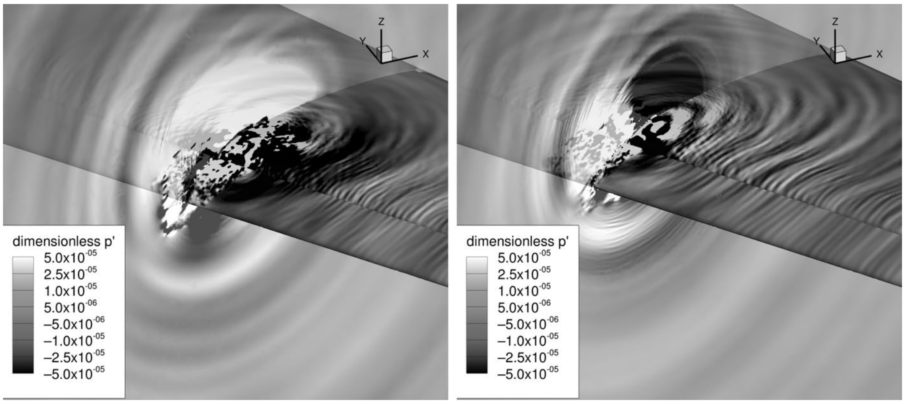

Fig. 13 Acoustic pressure contours for the slat track case #18 (left), and "clean slat" case #17 (right)

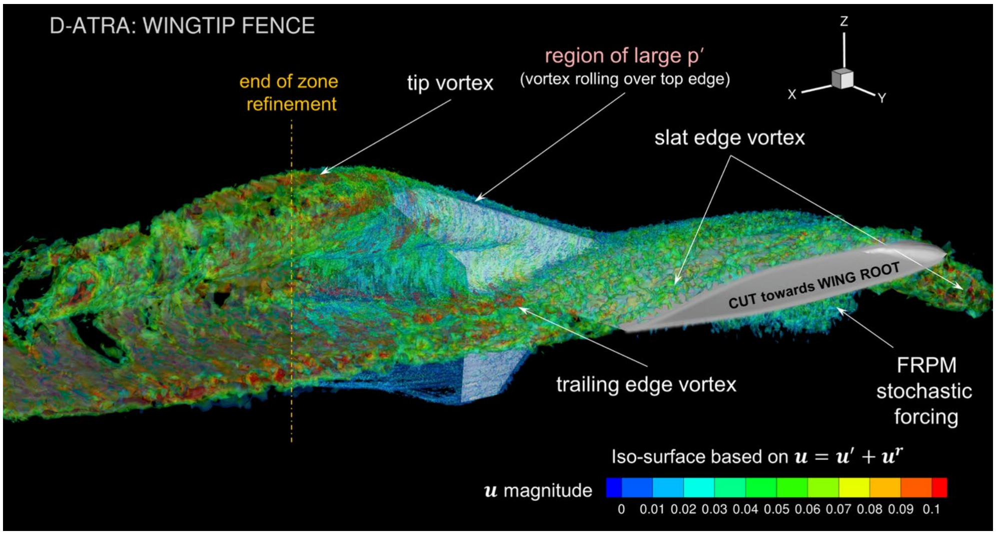

Fig. 14 D-ATRA wingtip fence iso-surface, showing instantaneous vortices

advection–diffusion–dissipation (FLAD) source. Figure 14 shows the iso-surface of instantaneous vorticity based on $\boldsymbol{u} = \boldsymbol{u}' + \boldsymbol{u}^r$ (see Sect. 2 noise sources), coloured by $\boldsymbol{u}$-magnitude. The stochastic FRPM forcing was applied upstream in a zone aligned with the wingtip fence. Interestingly, the stochastic motor, which is not responsible for production (that is caused by the mean gradient term), but instead the reshuffling of energy also makes the slat edge vortex to appear that is present in the RANS, which then convects over the wing and merges with trailing edge vortices. Notice the tip vortex development and much greater turbulence for the top half. Figure 15 shows the near-field acoustics of the broadband edge noise which is complex in nature and radiated in multiple directions.

There are several prominent noise sources due to vortex structure interaction: coming from the large vortex rolling over the top edge of the wingtip fence, also the trailing and slat edge noise. Those are mostly contributing to higher frequency bands in comparison to slat noise, in the range of 1.5 … 4 kHz.

4.4 Landing gear

4.4.1 Main gear

Landing gear simulations were performed with a finite difference PIANO-IBM (immersed boundary method) solver of DLR with the canonical stochastic (FLAD) source model, consisting of Eq. (10) together with the APE equations, Eqs. (6)–(7). In PIANO-IBM, a dispersion-relation-preserving (DRP) [22] finite difference scheme is employed with an explicit fourth-order Runge–Kutta time marching. PIANO-IBM is tailored to solve aeroacoustic problems with equations ranging from linear systems such as APE and LEE to formulations of higher complexity (e.g., FLAD), and to fully non-linear disturbance equations [23]. This leads to the capability of solving a full set of Navier–Stokes equations.

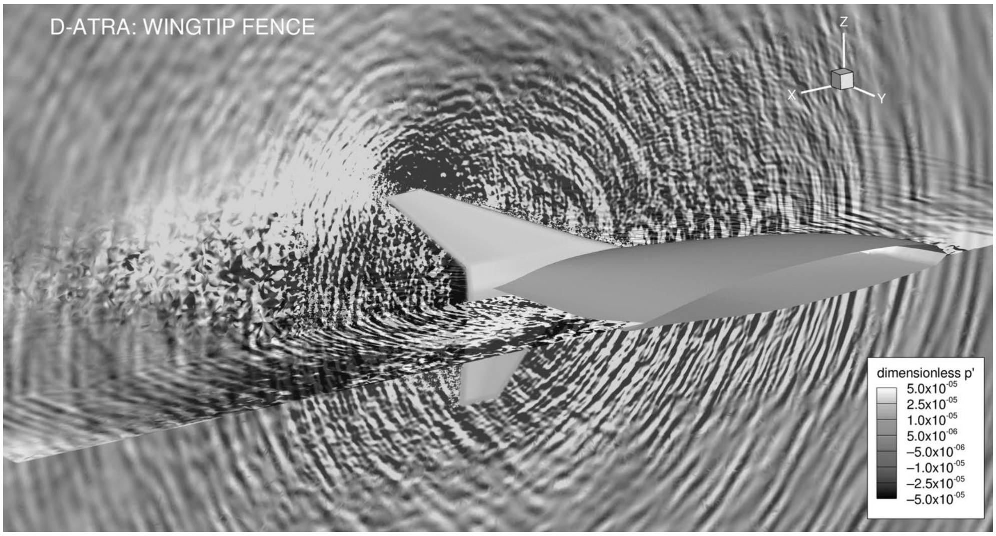

Fig. 15 D-ATRA wingtip fence contour slices, showing instantaneous pressure fluctuations

For performance reasons, usually the solver is used in perturbation mode with mean variables supplied from RANS, allowing to solve on full scale with a coarser near-wall resolution to that otherwise required, for example in a wall-modelled LES mode. In this work, a sharp interface IBM of Zhao et al. [24] is applied. First, the hierarchical Cartesian meshing blocks were created for the landing gear in a sub-domain of the entire aircraft with different levels of refinement. The CAA volume was meshed with 5488 blocks, consisting of 183 million grid points. The computational domain measures 19.5 m × 2.5 m × 7.5 m with 51 × 21 × 31 points per block (see Fig. 16a). The refinement is problem-specific, performed with stretched cuboid cells. Figure 16b shows the mirrored acoustic simulation for the main landing gear, case #9.

4.4.2 Nose gear

Figure 17 shows the iso-surface of Q-criterion coloured by the magnitude of velocity fluctuations for the nose landing gear (NLG), case #19. The NLG was computed with the canonical stochastic source model, equivalently to the MLG. The acoustic sources appear to be weaker for the NLG, which is in line with expectations. The acoustic signal was collected in time domain on a cylindrical closed surface around the landing gear. It remains to be verified if the noise levels are comparable to a “gear down” fly-over.

4.5 Inboard flap

The simulation was performed for fully deployed flaps, later referred to as “flaps full”. Unlike the slat noise, which is radiated predominantly downstream, the flap group emits noise directly below the wing, if not slightly upstream when fully deployed. Some important sources of noise are trailing edges, side edges, cavities, gaps, and flap cove. An FRPM volume region with a limited spanwise extent of 0.6 m was used for simulating a clean section of the flap, where the far-field noise was corrected for the actual flap extent (i.e., which is not included in any other source regions), using exactly the same procedure as for the “clean slat” noise simulations, $+10\log_{10}(\text{flap extent}/\text{patch width})$. The outboard flap noise was simulated separately as the angle of sweep is different, and thus, a proper reference for the outboard clean flap was required to avoid any overcorrection or crude assumptions. All other flap sources were modelled with *Source B*, where the near-field acoustics was propagated to a permeable FWH surface. There were no additional corrections applied to simulations, as they fully comply with the wind tunnel situation.

4.5.1 Wing root flap gap

The wing root flap gap is one of the major sources of noise due to a high deployment angle and a large flap chord, required for generating high lift. It inevitably results in an adverse effect of a highly turbulent flow in and around gaps being in contact with multiple edges, as the flow is accelerated through the slits between the wing and fuselage. Hence, a large volume box that fully encloses the slat cove, gap, and trailing edges was created and labelled as case #6. This volume box inevitably captures some of the flap noise, and hence, the region has to be excluded from the inboard flap extent used for correcting case #15, together with the fairing. Again, referring to Fig. 2, it is emphasised that flap sources must be carefully combined, instead of applying the

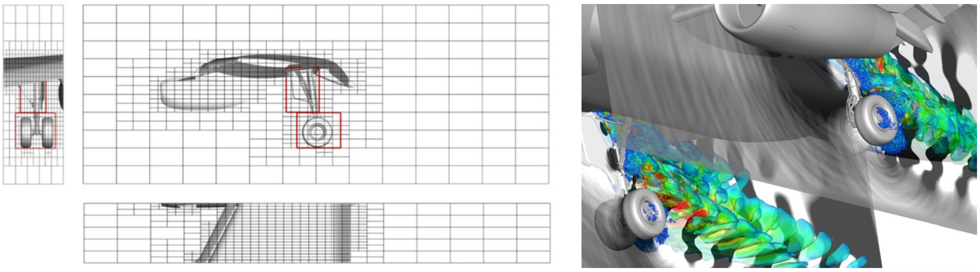

(a) Blocks

(b) Iso-surface

Fig. 16 MLG blocks; acoustic pressure contours and turbulent fluctuations for the MLG, case #9

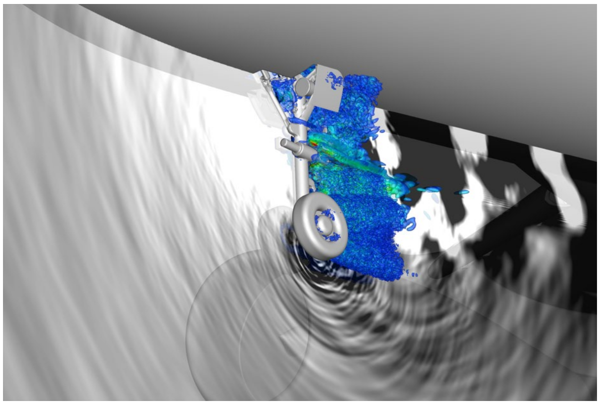

Fig. 17 Turbulent and acoustic fluctuations for the NLG, case #19

spanwise correction based on the overall flap length. Otherwise, it may result in errors of several decibels, mainly because stronger sources from compact regions become comparable in magnitude to distributed sources due to a large geometry.

4.5.2 Flap junction

Figure 18 shows the stochastic source domain together with instantaneous contours of acoustic pressure for the flap junction. The gap between the inboard and outboard flaps is covered by a rubber insert, and hence, this junction is not expected to be a source of excessive noise. In spite of this, case #7 is part of our acoustic modelling strategy, being a region of complicated turbulent flow.

4.6 Outboard flap

Figure 19 shows contours of instantaneous pressure for the outboard flap and other marked source domains. Similarly to the inboard flap, the spanwise correction to far-field noise is applied between the flap junction and side edge domains due to a limited spanwise extent used in the "clean flap" simulation.

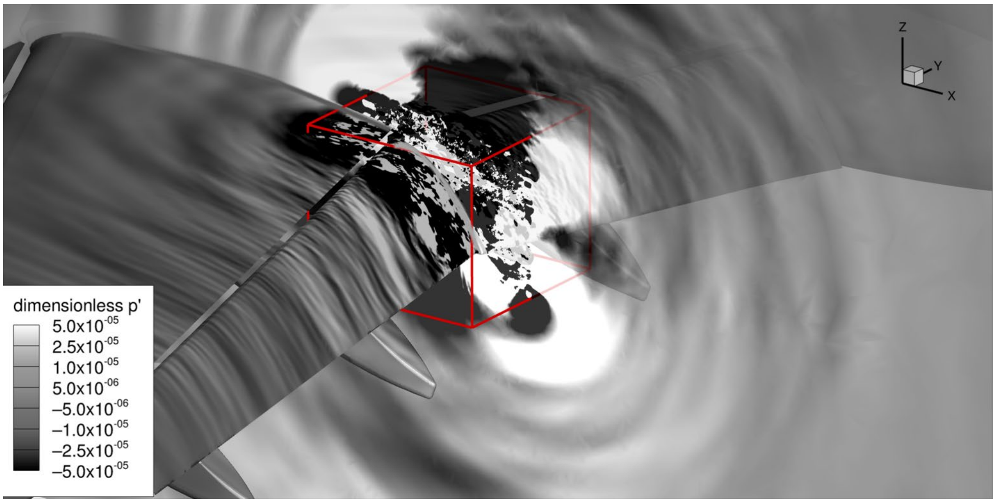

Fig. 18 Contours of instantaneous pressure fluctuations for the flap junction and the highlighted FRPM source domain

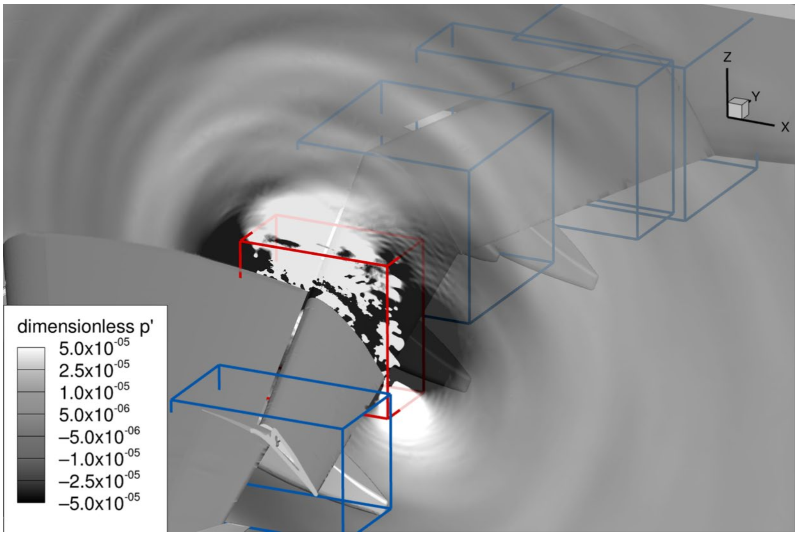

Fig. 19 Contours of instantaneous pressure for the outboard flap FRPM source domain (highlighted) along with the other flap group source domains

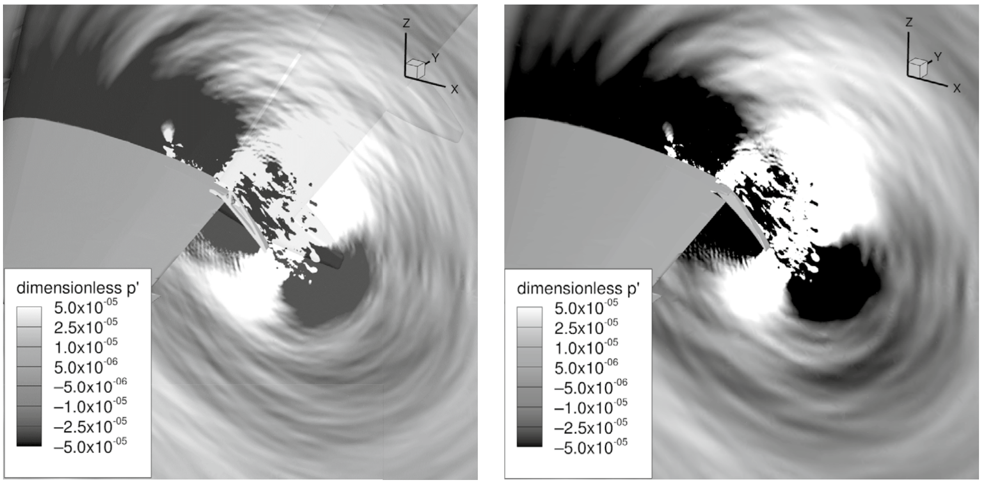

(a) Case #8 (b) Case #10

Fig. 20 D-ATRA outboard flap side edge noise at the same time instance

4.6.1 Side edge

Figure 20a and b show snapshots of instantaneous pressure contours at the same time instance, where the pressure waves are in phase. A higher frequency ripple effect can be seen for the baseline case #8 in comparison to a filled cavity side edge, case #10.

This suggests that the noise content will be different, at least for higher frequency bands. Figure 21 shows the 1/3 octave bands delta SPL [dB] footprints plotted at 100 m below the aircraft. It can be seen that a significant noise reduction is achieved for the “low noise” case #10 at 3174 Hz. The lower frequency bands, namely 250 Hz and 500 Hz, remain unaffected by this geometrical modification. Also, lower frequencies seem to be dominant in terms of absolute levels, but this could be explained as the source region includes a significant portion of the outboard flap. The side edge itself is a high-frequency source and the noise reduction achieved by closing the cavity is in line with expectations.

5 OASPL simulated noise and fly-over measurements

In the simulation, the acoustics was propagated on top of the RANS flow in the near-field, collected on permeable FW-H surfaces and integrated to a large far-field plane (400 m × 400 m) at $Z = -100$ m with a constant Mach number of 0.204. The reader could imagine a full-scale open wind tunnel with a fixed aircraft position and flow everywhere between the source and numerical

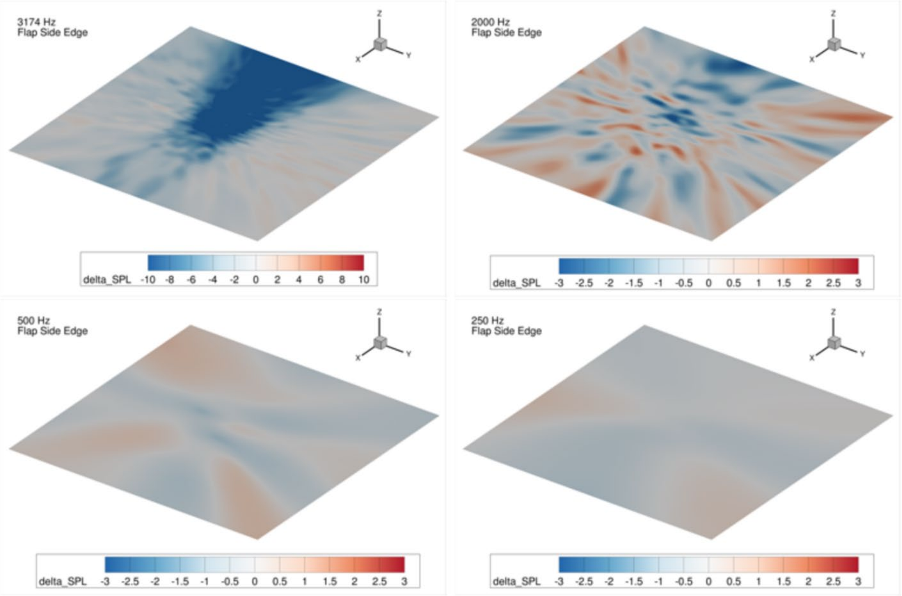

Fig. 21 1/3 Octave bands delta SPL [dB] between baseline case #8 and closed cavity case #10

microphones. In the fly-over, the D-ATRA aircraft is moving along its flight path, descending towards a runway, maintaining a low speed of 135 kt. at an altitude of approximately 600 ft. (with engines at idle) over a microphone grid with the dimensions of 220 m × 120 m, and then increasing thrust and accelerating away at a high polar angle relative to the observer. The ground microphones were placed over concrete slabs on the grass, and also installed over the runway. All microphones are stationary observers, recording p', with changing distances and angles to the source over time. The record naturally contains the Doppler effect and atmospheric attenuation. Notice that in both cases, the acoustic sources are subject to convective amplification but in the fly-over, the microphones do not experience any flow apart from a light breeze and for most part, acoustic propagation takes place in a medium at rest. This has to be corrected for to be comparable with the simulation. Below is our summary of the most important processing steps followed for obtaining the fly-over noise footprints:

1. The microphone coordinates are assigned relative to the camera position and the source location is determined from GPS data of the aircraft, synchronised in time with the camera position.
2. The data are de-Dopplerised by computing the true aircraft position as well as the retarded time.
3. The retarded time is no longer equidistant, but it is again made equidistant by interpolating pressure data with a new fixed sampling rate. The reconstructed uniform signal is used in the fast Fourier transform calculation.
4. **Microphone corrections** are applied due to the ground effect.
5. **Distance correction** is applied to get the footprint at $Z = -100$ m.
6. **Atmospheric attenuation** is removed for consistency with the simulation
7. **Convective flow effects** applied to match the wind tunnel situation/simulation.

Figure 22 shows the OASPL levels at the ground derived from the average over several fly-overs (labelled experiment) and simulation, respectively. This is a snapshot where the D-ATRA aircraft is located at $\{0; 0\}$ with its nose pointing in the negative x-direction. In both the experimental and numerical data, very low frequencies (up to 50 Hz) were discarded from the analysis. The simulated footprint was mirrored to account for both wings, whereas the experimental footprints were averaged over the centreline. The OASPL footprints are plotted on a half-plane for a 10 dB range in 0.5 dB increments. As can be seen, the results are in excellent agreement, well within the measurement tolerance everywhere across the field. Figure 23 shows the absolute noise level comparison along the centreline, where slight differences can be seen on a finer scale. Notice that maximum levels are obtained slightly downstream relative to the aircraft position. The “Gear Down” simulation has a slightly higher peak noise level (≈ 1.5 dB over the measurement), but which is still less than 3 dB in comparison to the “Gear Up” simulation, meaning that the installed landing gear is less noisy than the D-ATRA airframe for the given conditions. This finding is consistent between the experiment and simulation results. In Fig. 24, the gear causes more upstream noise radiation which can be clearly detected when comparing the footprints to those

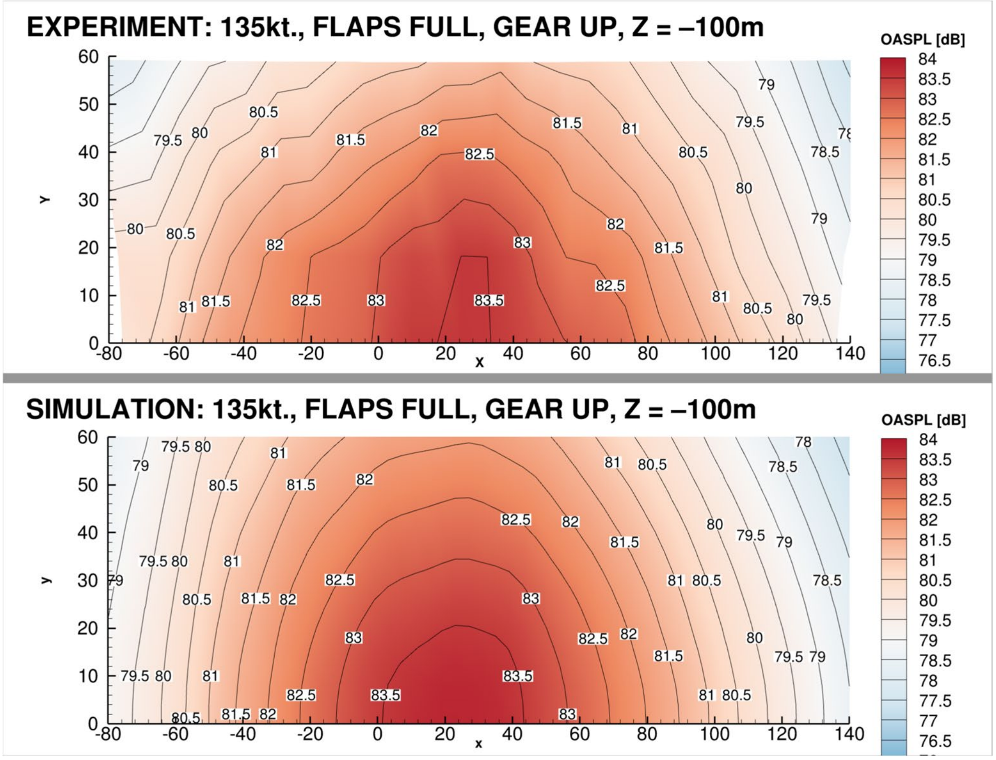

Fig. 22 OASPL [dB] footprint; baseline; gear up

Fig. 23 OASPL [dB] comparison along the centreline

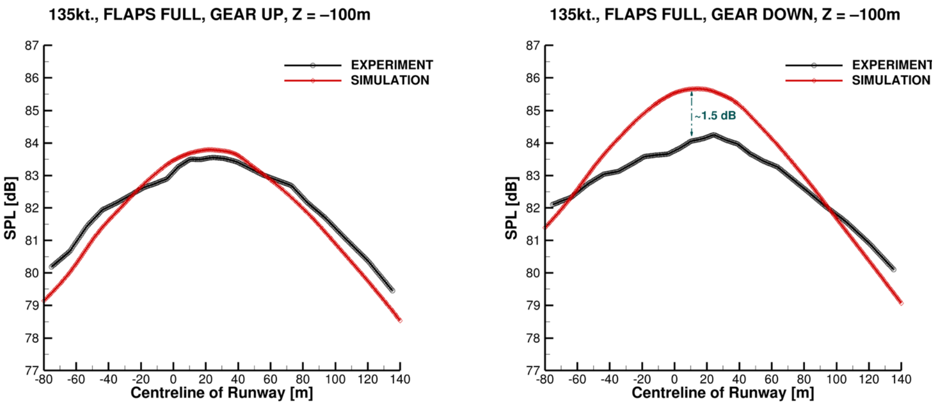

(a) Gear UP

(b) Gear DOWN

in Fig. 22. At large polar angles in the forward arc, the experimentally determined levels are 1–1.5 dB higher with the gear deployed when compared to the “Gear Up” measurements (based on 6 fly-over averages), and in the simulation, the deltas are 2–2.5 dB. A slight difference is expected between fly-over passes. The landing gear simulation based on the canonical stochastic model was performed for the first time and produced accurate levels and directivity, within the tolerance of 3 dB to the measurement. This shows that the model did not require any specific adjustments, beyond a completely standard setup. The airframe noise is examined in greater details by comparing 1/3 octave bands. Figures 25, 26, 27, 28, 29 and 30 in the Appendix show that trends are closely reproduced and most footprints are within the measurement tolerance with the exception of band 3150 Hz, where differences are visible upstream on the periphery. The source of increased upstream levels at 3150 Hz in the fly-over measurements remains unclear.

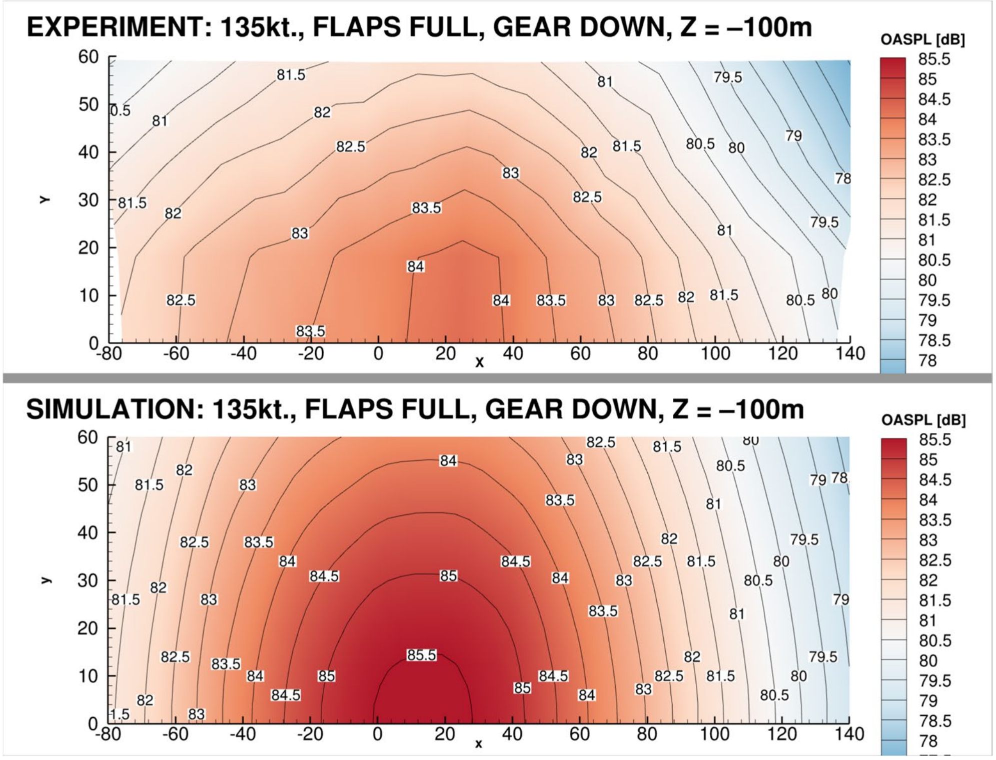

Fig. 24 OASPL [dB] footprint; baseline; gear down

6 Conclusion

The simulation was performed for the D-ATRA A320 aircraft of DLR in landing configuration and compared to fly-over measurements. The measured and simulated footprints of the overall SPL agreed very closely for retracted and deployed landing gear configurations. A close agreement was achieved at the centreline of the runway, with simulated levels reported to be well within the measurement tolerance. Additionally, the 1/3 octave band comparison provided insights into the noise frequency content and directivity from different sources. In the simulation with the retracted landing gear and where jet noise is assumed negligible (not simulated), the main noise source mechanism can be attributed to the extended slat, whose directivity characteristics can be described by a dipole placed vertically on the slat chord at the trailing edge of the slat. With the slat angle of incidence, the runway inclination angle, and the angle of attack of the aircraft, the maximum of sound radiation can be estimated at a polar angle of approximately $\phi = 114°$, which is in very good agreement with the simulation results. Also, flap noise is relevant due to the sheer size of components, and of course, the landing gear which shifts the noise peak closer to the origin and slightly upstream. The canonical stochastic source model performed well for an initial trial, the accuracy of which depends on the RANS resolution. Any sensitivity of the model based on the resolution of mean flow gradients is yet to be studied. There are several open questions related to the side edge noise mechanisms that become relevant at higher frequencies (3000 Hz), if those are properly reproduced by *Source B*. It is planned to fully switch to the canonical stochastic source model for all regions, by first validating it against LES simulations and wind tunnel measurements on a model scale. By far, the biggest computational expense was solving the near-field acoustics propagation for each source with the DG method. However, a significantly lower computational effort is required in comparison to, e.g., a zonal WM-LES approach, where obtaining quality flow on full-scale remains extremely challenging. On the contrary, the zonal approach used in combination with stochastically derived sources is shown to be promising for design, as any validated sources (unmodified regions) could be kept fixed, which enables us to capture fine noise differences for any section of a modified airframe with a short turnaround time.

Appendix

See Table 1 and Figs. 25, 26, 27, 28, 29 and 30.

Table 1 Simulation parameters

Source	Case	Name	Cores^1	CAA mesh^2	CPUh (k)	WCT (h)^3	Mem (TB)	Real time (s)^4
B	1	Slat edge, gap, track I	1280	2,5	52,5	41,0	0.14	0.294
B	2	Slat track II	1280	3,3	62,7	49,0	0.16	0.290
B	3	Slat track V	1280	2,1	47,0	36,7	0.14	0.294
B	4	Pylon junction	1280	3,3	71,9	56,2	0.16	0.294
FLAD	5	Slat edge and wingtip fence	2560	9,4	153,6	60,0	0.25	0.294
B	6	Flap edge/gap	1280	4,1	90,9	71,0	0.16	0.294
B	7	Flap junction	1280	4,2	86,1	67,3	0.16	0.294
B	8	Flap side edge	1280	2,7	62,8	49,1	0.15	0.294
FLAD^5	9	MLG	5490	182	241.6	44,0	0.85	0.400
B	10	Flap side edge (LN)	1280	2,9	61,1	47,7	0.15	0.294
B	11	Inboard slat	1280	5,0	102,4	80,0	0.20	0.290
B	12	Track III	1280	2,8	57,6	45,0	0.15	0.294
B	13	Track IV	1280	2,8	57,9	45,3	0.15	0.294
B	14	De-icing tube	2560	4,9	111,4	43,5	0.20	0.306
B	15	Inboard flap	1280	3,0	79,1	61,8	0.18	0.294
B	16	Outboard flap	1280	3,3	68,5	53,5	0.17	0.265
B	17	Outboard slat	1280	3,2	67,2	52,5	0.16	0.294
B	18	Outboard slat track	1280	2,3	74,6	58,3	0.13	0.530
FLAD^5	19	NLG	5490	160	220,0	40,0	0.80	0.400
Total		Efficiency mode	5490		1768,9	322,2	0.85	≈ 0.3
		Performance mode	35,300		1768,9	50,1	4,46	≈ 0.3

[1] 1 computational node consists of 2 × AMD EPYC 7601 (64 cores) 128 GB DDR4 RAM or 2 × AMD EPYC 7702 (128 cores) 256 GB DDR4 RAM. [2] Number of high-order unstructured mesh cells per zone (millions). [3] Wall clock time. [4] CAA only (inc. FWH IO). [5] PIANO-IBM (FD) code

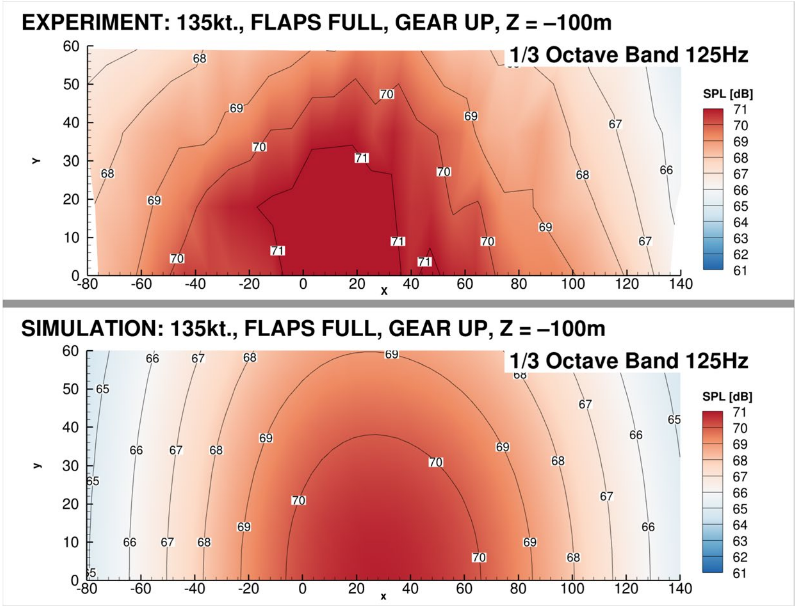

Fig. 25 Third octave band 125 Hz, SPL [dB] footprint; baseline; gear up

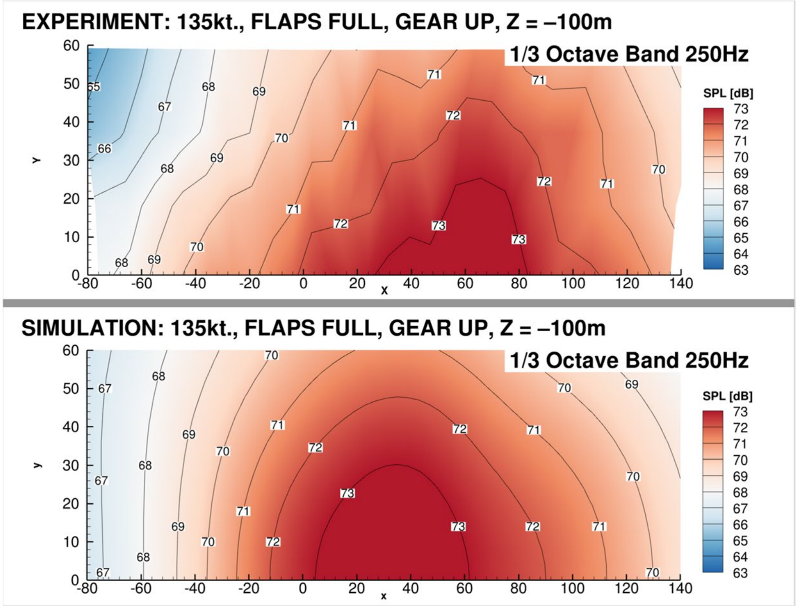
EXPERIMENT: 135kt., FLAPS FULL, GEAR UP, Z = –100m

1/3 Octave Band 250Hz

SIMULATION: 135kt., FLAPS FULL, GEAR UP, Z = –100m

1/3 Octave Band 250Hz

Fig. 26 Third octave band 250 Hz, SPL [dB] footprint; baseline; gear up

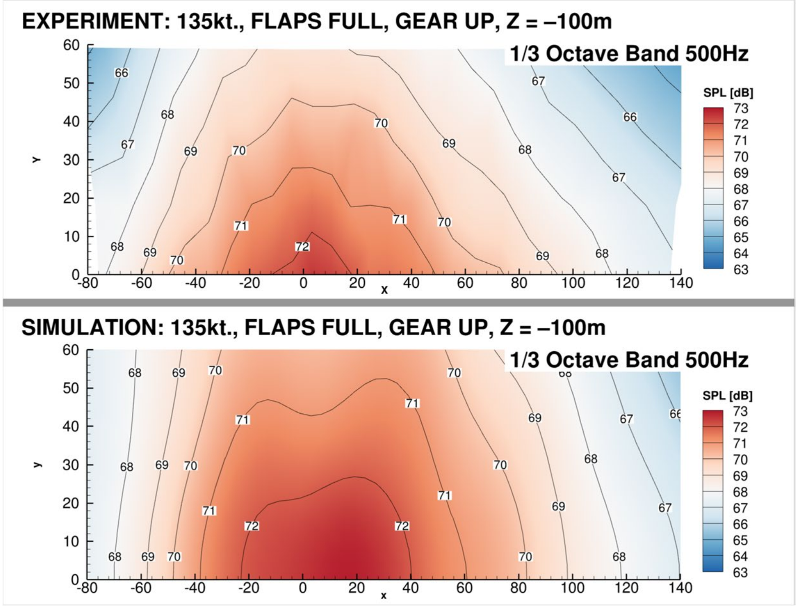
EXPERIMENT: 135kt., FLAPS FULL, GEAR UP, Z = –100m

1/3 Octave Band 500Hz

SIMULATION: 135kt., FLAPS FULL, GEAR UP, Z = –100m

1/3 Octave Band 500Hz

Fig. 27 Third octave band 500 Hz, SPL [dB] footprint; baseline; gear up

Fig. 28 Third octave band 1000 Hz, SPL [dB] footprint; baseline; gear up

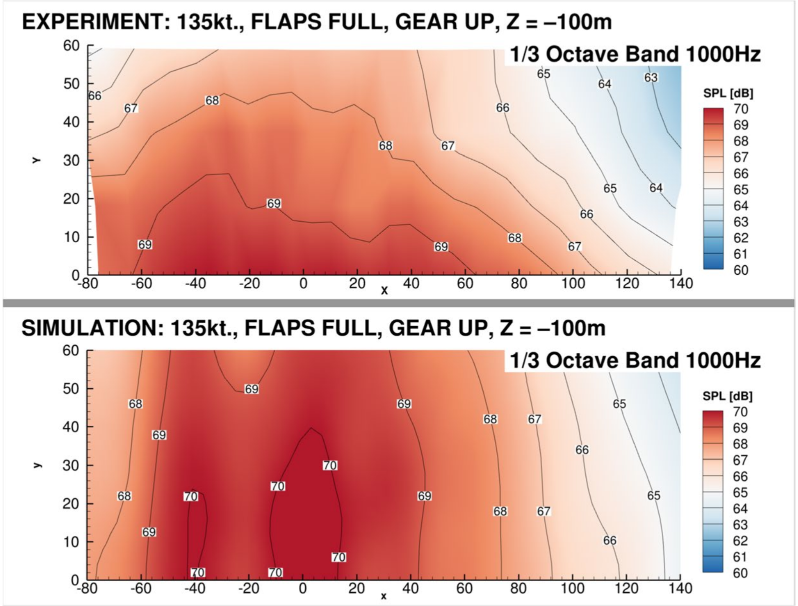
EXPERIMENT: 135kt., FLAPS FULL, GEAR UP, Z = –100m

1/3 Octave Band 1000Hz

SIMULATION: 135kt., FLAPS FULL, GEAR UP, Z = –100m

1/3 Octave Band 1000Hz

Fig. 29 Third octave band 2000 Hz, SPL [dB] footprint; baseline; gear up

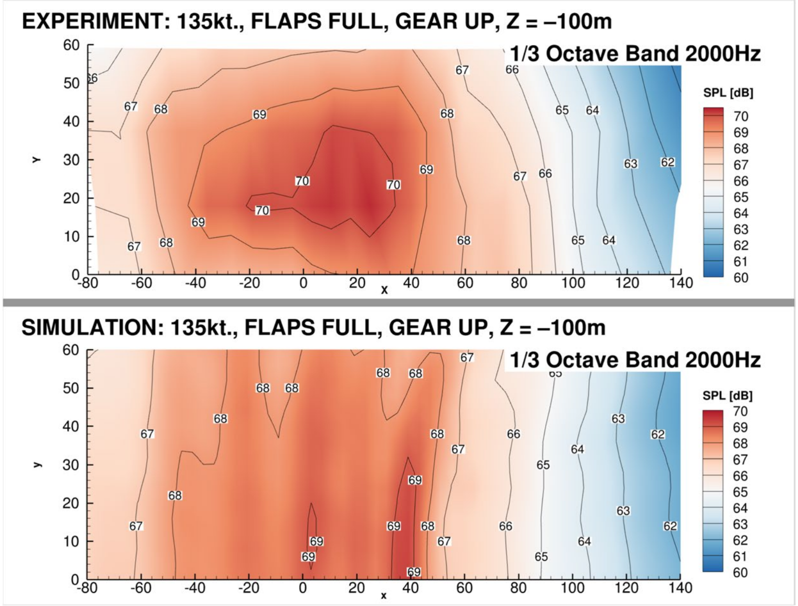
EXPERIMENT: 135kt., FLAPS FULL, GEAR UP, Z = –100m

1/3 Octave Band 2000Hz

SIMULATION: 135kt., FLAPS FULL, GEAR UP, Z = –100m

1/3 Octave Band 2000Hz

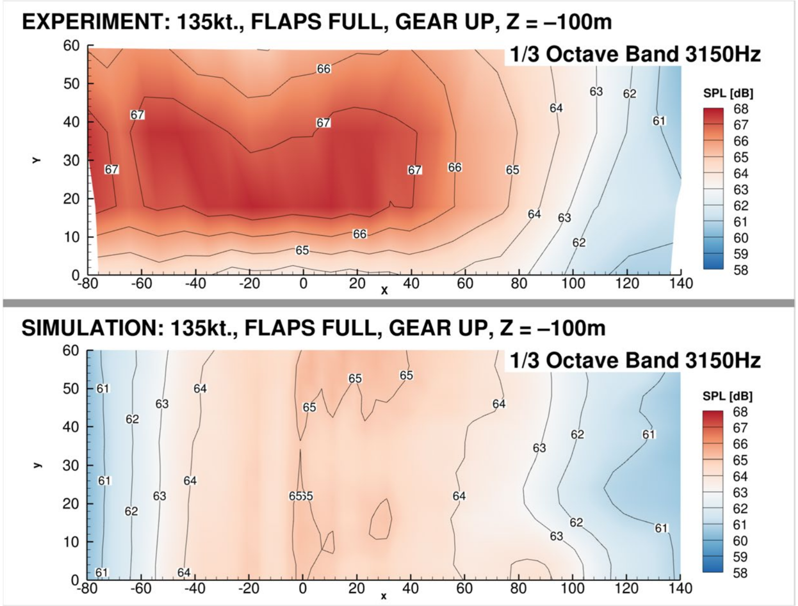

Fig. 30 Third octave band 3150 Hz, SPL [dB] footprint; baseline; gear up

Acknowledgements The work has been conducted as part of the internal DLR project SIAM. The authors thank Florian Schmidt and Dennis Keller from AS-TFZ, DLR for providing their RANS data for the D-ATRA aircraft. The authors gratefully acknowledge the scientific support and HPC resources provided by the German Aerospace Center (DLR). The HPC system CARA is partially funded by "Saxon State Ministry for Economic Affairs, Labour and Transport" and "Federal Ministry for Economic Affairs and Climate Action".

Author contributions S.P. wrote the main manuscript text and performed airframe noise simulations. M.M. helped with the FWH code, post-processing of numerical results and comparisons to fly-over. R.E. provided important intellectual content, heavily involved in equations engineering. J.W.D. made substantial contributions to the conception of the work, involved in results analysis and comparisons, critically revised the work and approved the version to be published. J.D. performed landing gear simulations with PIANO-IBM code. M.P.-P. involved in data comparison and data analysis on the experimental side, ensuring that the measured data are accurate and correctly presented. D.A. involved in measurements post-processing and fly-over data corrections.

Funding Open Access funding enabled and organized by Projekt DEAL.

Data availability No datasets were generated or analysed during the current study.

Declarations

Conflict of interest The authors declare no competing interests.

References

1. ACARE: Vision; Flightpath 2050, 2023-11-13 (2023)
2. Siller, H.A., Bassetti, A., Hage, W., Funke, S.: Measurements of the noise emitted by the v2500 engines in flight and in static measurements on the ground. In: 23rd AIAA/CEAS Aeroacoustics Conference, 5–9 June, Denver, CO, USA (2017). https://doi.org/10.2514/6.2017-3844
3. Pott-Pollenske, M., Almoneit, D., Buchholz, H.: Low noise ATRA—an aircraft noise reduction study based on retro-fit technologies. In: AIAA Aviation 2021 Forum, 2–6 August, VIRTUAL (2021). https://doi.org/10.2514/6.2021-2117
4. Schwamborn, D., Gerhold, T., Heinrich, R.: The DLR TAU-Code: recent applications in research and industry. In: Wesseling, P., Oñate, E., Périaux, J. (eds.) European Conference on Computational Fluid Dynamics, ECCOMAS CFD. TU Delft (2006). http://proceedings.fyper.com/eccomascfd2006/documents/619.pdf
5. Khorrami, M.R., Fares, E., Casalino, D.: Towards full aircraft airframe noise prediction: lattice Boltzmann simulations. In: 20th AIAA/CEAS Aeroacoustics Conference, 16–20 June, Atlanta, GA, USA (2014). https://doi.org/10.2514/6.2014-2481
6. Appelbaum, J., Duda, B., Fares, E., Khorrami, M.R.: Airframe noise simulations of a full-scale aircraft. In: 24th AIAA/CEAS Aeroacoustics Conference, 25–29 June, Atlanta, GA, USA (2018). https://doi.org/10.2514/6.2018-2973
7. Khorrami, M.R., König, B., Fares, E., Ribeiro, A.F.P., Czech, M., Ravetta, P.A.: Airframe noise simulations of a full-scale large civil transport in landing configuration. In: AIAA Aviation 2021 Forum, 2–6 August, VIRTUAL (2021). https://doi.org/10.2514/6.2021-2161
8. CS-Group: ProLB: High-fidelity CFD in Exceptional Turnaround Times. https://prolb-cfd.com. Accessed 17 Nov 2023

9. Ewert, R., Dierke, J., Siebert, J., Neifeld, A., Appel, C., Siefert, M., Kornow, O.: Caa broadband noise prediction for aeroacoustic design. Journal of Sound and Vibration **330**, 4139–4160 (2011). https://doi.org/10.1016/j.jsv.2011.04.014
10. Ewert, R., Proskurov, S., Dierke, J.: Reformulated flow-acoustics splitting for RANS/CAA based acoustic metrics: tip leakage flow problem. In: AIAA AVIATION 2023 Forum, 12–16 June, San Diego, CA, USA (2023). https://doi.org/10.2514/6.2023-3500
11. Reiche, N., Lummer, M., Ewert, R., Delfs, J.W.: Towards high-lift noise from fast multipole BEM with anisotropic synthetic turbulence sources. In: 21th AIAA/CEAS Aeroacoustics Conference, 22–26 June, Dallas, TX, USA (2015). https://doi.org/10.2514/6.2015-2672
12. Ewert, R., Schröder, W.: Acoustic perturbation equations based on flow decomposition via source filtering. J. Comput. Phys. **188**, 365–398 (2003). https://doi.org/10.1016/S0021-9991(03)00168-2
13. Ffowcs Williams, J.E., Hawkings, D.L.: Sound generation by turbulence and surfaces in arbitrary motion. Philos. Trans. R. Soc. Lond. A: Math. Phys. Eng. Sci. **264**(1151), 321–342 (1969). https://doi.org/10.1098/rsta.1969.0031
14. Powell, A.: Theory of vortex sound. J. Acoust. Soc. Am. **36**(1), 177–195 (1964). https://doi.org/10.1121/1.1918931
15. Ewert, R., Kreuzinger, J.: Hydrodynamic/acoustic splitting approach with flow-acoustic feedback for universal subsonic noise computation. J. Comput. Phys. (2021). https://doi.org/10.1016/j.jcp.2021.110548
16. Ewert, R.: Canonical stochastic realization of turbulent sound sources via forced linear advection–diffusion–dissipation equation. In: 22nd AIAA/CEAS Aeroacoustics Conference, 30 May–1 June, Lyon, France (2016). https://doi.org/10.2514/6.2016-2965
17. Ewert, R.: RPM—the fast random particle-mesh method to realize unsteady turbulent sound sources and velocity fields for CAA applications. In: 13th AIAA/CEAS Aeroacoustics Conference, 21–23 May, Rome, Italy (2007). https://doi.org/10.2514/6.2007-3506
18. Wilcox, D.C.: Turbulence Modeling for CFD, 3rd edn. DCW Industries, Inc., California (2006)
19. Menter, F.R.: Eddy viscosity transport equations and their relation to the k-ϵ model. Fluids Eng. **119**(4), 876–884 (1997). https://doi.org/10.1115/1.2819511
20. Reiche, N., Ewert, R., Delfs, J.W.: Realization of arbitrary vorticity spectra using generic stochastic turbulence. In: 22nd AIAA/CEAS Aeroacoustics Conference, 30 May–1 June, Lyon, France (2016). https://doi.org/10.2514/6.2016-2964
21. Young, I.T., van Vliet, L.J.: Recursive implementation of the gaussian filter. Signal Process (1995). https://doi.org/10.1016/0165-1684(95)00020-E
22. Tam, C.K.W., Webb, J.C.: Dispersion-relation-preserving finite difference schemes for computational acoustics. J. Comput. Phys. **107**(2), 262–281 (1993). https://doi.org/10.1006/jcph.1993.1142
23. Dierke, J., Mößner, M., Ewert, R., Delfs, J.: Wind tunnel vs. free flying aircraft: comparison of UHBR jet installation noise using zonal LES on octree-cartesian grids. In: 30th AIAA/CEAS Aeroacoustics Conference, 4–7 June, Rome, Italy (2024). https://doi.org/10.2514/6.2024-3411
24. Zhao, C., Yang, Y., Zhang, T., Dong, H., Hou, G.: A sharp interface immersed boundary method for flow-induced noise prediction using acoustic perturbation equations. Comput. Fluids (2021). https://doi.org/10.1016/j.compfluid.2021.105032